Eddy-Current Imaging with Nitrogen-Vacancy Centers in Diamond

Georgios Chatzidrosos,[1,*] Arne Wickenbrock,[1] Lykourgos Bougas,[1] Huijie Zheng,[1] Oleg Tretiak,[1] Yu Yang,[2] and Dmitry Budker[1,3,4,5]

[1] *Johannes Gutenberg-Universität Mainz, 55128 Mainz, Germany*
[2] *University of Science and Technology of China, Hefei, 230026, China*
[3] *Helmholtz Institut Mainz, 55099 Mainz, Germany*
[4] *Department of Physics, University of California, Berkeley, California 94720-7300, USA*
[5] *Nuclear Science Division Lawrence Berkeley National Laboratory, Berkeley, California 94720, USA*

(Received 5 October 2018; revised manuscript received 10 December 2018; published 30 January 2019)

We demonstrate microwave-free eddy-current imaging using nitrogen-vacancy centers in diamond. By detecting the eddy-current+induced magnetic field of conductive samples, we can distinguish between different materials and shapes and identify structural defects. Our technique allows the discrimination of different materials according to their conductivity. The sensitivity of the measurements is calculated as 8×10^5 S/m $\sqrt{\text{Hz}}$ at 3.5 MHz for a cylindrical sample with radius $r_0 = 1$ mm and height $h = 0.1$ mm (volume approximately 0.3 mm^3) at a distance of 0.5 mm. In comparison with existing technologies, the diamond-based device exhibits a greater bandwidth and spatial resolution. In particular, we demonstrate a flat frequency response from 0 Hz to 3.5 MHz and a spatial resolution of 348 ± 2 μm.

DOI: 10.1103/PhysRevApplied.11.014060

I. INTRODUCTION

Magnetic induction measurements have proven to be useful in biomedicine [1], security and surveillance [2,3], and testing of materials [4]. Magnetic induction imaging works by detecting magnetic fields produced by eddy currents. When a material is placed in an alternating magnetic field (primary field), electric fields will be induced in the material, causing eddy currents to flow. These in turn will produce a secondary magnetic field, which can be detected along with the primary field. The secondary field depends on the material's properties and shape, as well as the skin depth of the primary field. Eddy-current detection is commercially available with coil-based devices (e.g., Zetec MIZ-22). Recently it has also been demonstrated with vapor-cell magnetometers [5–7].

Here we demonstrate eddy-current imaging using magnetic sensing with nitrogen-vacancy (N-V) centers in diamond. Compared with other sensors, diamond-based devices operate over a wide temperature range and may have nanoscale resolution [8–10] with high sensitivity [11,12] and wide bandwidth [12]. The present eddy-current measurements are performed with an all-optical N-V magnetometer. The device has a bandwidth of 3.5 MHz and a spatial resolution of 348 μm.

*gechatzi@uni-mainz.de

II. EXPERIMENTAL SETUP

The N-V-center energy levels are presented in Fig. 1(a). The ground and excited electronic spin-triplet states of the N-V are $^3A_2$ and ^3E, respectively, with the transition between them having a zero-phonon line at 637 nm. Additionally, there are two singlet states. Optical transition rates in the system are spin independent; however, the probability of nonradiative intersystem crossing from ^{3}E to the singlets is several times higher for $m_s = \pm 1$ than for $m_s = 0$ [13]. As a consequence, under continuous illumination with green pump light (532 nm), N-V centers are prepared in the $^3A_2$ $m_s = 0$ ground-state sublevel and in the metastable ^1E singlet state. The population in the $^3A_2$ $m_s = 0$ state is then excited by the green light and decays back, emitting red photoluminescence (PL).

The setup consists of a microwave-free diamond magnetometer in ac mode, a driving coil to induce eddy currents and a three-dimensional- (3D-) translation stage to make spatially dependent eddy-current measurements; that is, to create a conductivity image. The setup is shown in Fig. 1(b). The diamond used for this sensor is a type-Ib, (111)-cut, high-pressure-and-high-temperature-grown sample, purchased from Element Six. Its dimensions are $3 \times 3 \times 0.400$ mm^3. The initial nitrogen concentration of the sample was specified as less than 110 ppm. The sample is irradiated with 14-MeV electrons at a dose of 10^{18} cm^{-2} and then annealed at 700 °C for 3 h. Green light is provided to the setup by a diode-pumped solid-state laser (Laser Quantum, gem 532). The power of the laser is stabilized

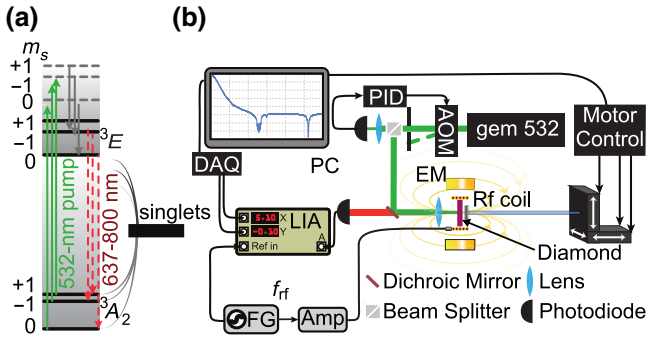

FIG. 1. (a) Relevant N-V-center energy levels and transitions. Solid green and red lines indicate excitations, dashed lines indicate radiative transitions, and solid gray lines indicate nonradiative transitions. (b) The experimental setup. AOM, acousto-optic modulator; DAQ, data acquisition; FG, function generator; PC, personal computer; PID, proportional-integral-derivative controller.

with an acousto-optic modulator (ISOMET 1260C with an ISOMET 630C-350 driver) controlled with a proportional-integral-derivative controller (SRS SIM960). The light is focused on the diamond with a 50-mm lens. Before being detected by a photodiode (Thorlabs PDA36A-EC), the PL is filtered with a dichroic mirror. The samples to be imaged are attached to a 24-cm nonconductive rod that is screwed onto a motorized, computer-controlled, 3D-translation-stage system (Thorlabs MTS25-Z8). With use of the translation stage, the samples are moved in front of the diamond. The eddy current inducing a magnetic field is produced with a function generator (Tektronix AFG 2021), ranging from 2 Hz to 4 MHz. The signal is supplied to a coil placed around the diamond (rf coil) with five turns and 3.4-mm diameter. It is made from 0.05-mm-diameter copper wire.

The all-optical magnetometry scheme to detect oscillating magnetic fields used here requires a homogeneous background field, which is provided by an electromagnet (EM). Both the diamond and the rf coil are placed inside the bore of the custom-made EM. The magnet consists of approximately 200 turns wound with a rectangular-cross-section (1.4×0.8 mm^2) wire around a 5 cm-diameter bore. The coil is wound on a water-cooled copper mount, and produces a background field of 2.9 mT per ampere supplied. A current of up to 55 A is provided by a Keysight N8737A power supply. A lock-in amplifier (LIA) (SRS SR865), referenced at the eddy-current frequency, detects the amplitude (R) and phase (θ) of the PL modulation. R and θ are recorded with a computer along with the position of the 3D-translation stage.

III. MAGNETOMETRY

The detection of magnetic fields commonly requires the use of microwaves to manipulate the spin state of the N-V ensemble [12]. However, in close proximity to conducting materials, the amplitude and phase of the microwaves are affected. For this reason we developed microwave-free detection techniques [14,15] that make use of different cross-relaxation and/or quenching mechanisms at various magnetic fields applied to diamond. We demonstrate the mechanism with an EM, but in a miniaturized device, this could be replaced by a carefully chosen permanent magnet.

PL by the N-V centers displays several features discussed in the literature as a function of a magnetic field [14–19], which can be used for magnetometry. Figure 2(a) presents normalized PL measurements as a function of the background magnetic field at different alignments of the magnetic field relative to the N-V axis. Figure 2(b) shows the corresponding amplitude of the PL oscillation due to the oscillating magnetic fields, R, as measured with a LIA component from the LIA. We investigate three different areas: α, the slope from 0 to approximately 25 mT; β, the cross-relaxation features around 50 mT; and γ, the

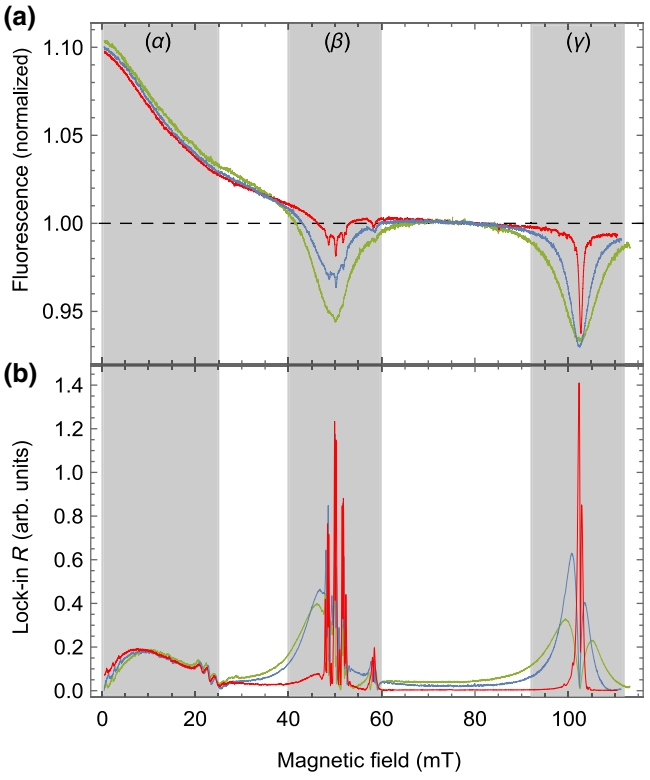

FIG. 2. (a) Fluorescence as a function of magnetic field at different alignments (up to approximately 5°) between the N-V axis and the magnetic field axis. The smallest misalignment is represented by the red trace and the biggest misalignment is represented by the green trace. The data are normalized to the PL at 80 mT. (b) Lock-in amplifier R component for the same alignments between the N-V axis and the magnetic field axis, with an applied magnetic field modulation of 60 kHz and an amplitude of 50 μT. The shaded areas α, β, and γ represent magnetic field values at which we performed ac magnetometry.

ground-state-level anticrossing feature at 102.4 mT. To perform the measurements, we apply a bias field and maximize R for the different features. While R is maximized due to the quadratic shape of the feature, there is not sensitivity to small changes in the bias field. However, because demodulation is done at the frequency of the eddy current with a lock-in amplifier, there is sensitivity to ac field changes.

As shown in Fig. 2(b) the maximum R is obtained at the ground-state-level anticrossing for the red trace. However, as reported in the literature [14], this feature is sensitive to misalignment. To make the sensor more robust to misalignment, we perform the measurements at area α. Even though area α is less sensitive, it allows robustness, which will be useful in a portable device. Instead of requiring a highly homogeneous magnetic field, a standard permanent magnet could bias the field. The smaller field value additionally facilitates implementation in a miniaturized sensor and requires less power dissipation if an EM is used.

For eddy-current detection measurements a broad bandwidth is important because the frequency of the primary field determines its penetration depth into the sample under study. The penetration depth in turn provides information about the geometry, thickness, and material of the sample. Hence, to optimize images of different-thickness materials, a wide frequency range is beneficial. Furthermore, higher frequencies enhance the response and make it possible to image materials with lower conductivity. Figure 3 shows the normalized eddy-current response as a function of frequency to characterize the sensor's bandwidth. The blue trace is taken at a pump intensity $I = 20$ W/mm^2, the orange trace is taken at $I = 180$ W/mm^2, and the green trace is taken at $I = 600$ W/mm^2, which corresponds to the saturation intensity for the probed N-V volume. The inset shows the normalized PL of the N-V as a function of pump-light intensity. The intensities at which the data are taken are represented in the inset by the corresponding colors from the main plot. The measurements are fitted with first-order low-pass-filter functions. As illustrated in Fig. 3, the bandwidth can be tuned by our varying the laser-light intensity and by our changing the alignment between the N-V axis and the magnetic field, which affects the mixing of the N-V $m_s = 0$ and $m_s = -1$ states [14]. We demonstrate a maximum bandwidth of approximately 3.5 MHz.

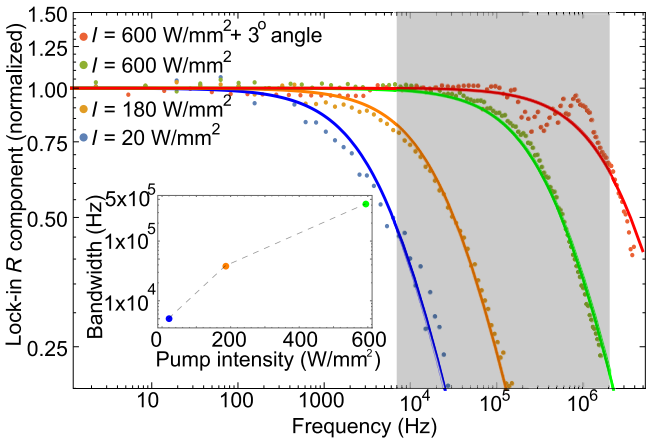

FIG. 3. Eddy-current response as a function of frequency. The blue, orange, and green measurements show the bandwidth of the device for different pump-power intensities. The red measurement is taken at saturation pump intensity and with 3° misalignment between the N-V axis and the magnetic field axis. The shaded area between 7 kHz and 2 MHz represents the maximum reported bandwidth of current atomic based sensors used for eddy-current imaging [7,20]. The inset shows the bandwidth of the magnetometer versus intensity with the corresponding colors of the traces.

IV. SPATIAL RESOLUTION

One of the advantages of N-V-based sensors is their spatial resolution. For eddy-current imaging, for a constant conductivity, the smaller a material is, the smaller the amplitude of the secondary field it produces. As a test of spatial resolution, we image 15 1-mm-diameter 35-μm-thick disks made of aluminum. The amplitude and phase responses of the magnetic field sensor caused by these disks are shown in Fig. 4. Both the disks and the distance between them, which is submillimeter, are clearly visible. Covering the pattern with aluminum foil adds an offset but does not significantly alter the eddy-current image patterns shown in Figs. 4(a) and 4(c).

Figure 5 shows the average cross section of the 15 1-mm disks imaged in Fig. 4. Using the average detected cross-section data, we deconvolute them with a square function, searching for a Gaussian-function kernel that would recreate the experimental results. The kernel provides information about the disks' width. In Fig. 5 the red plot signifies the disks' width of 1 mm as a square function, the blue dots are the experimental data, the green trace represents the Gaussian-function kernel, and the blue trace represents convolution result for the red and green traces. The amplitudes of all the traces are normalized to unity for representation in the Fig. 5. The Gaussian-kernel full width at half-maximum is 348 ± 2 μm, which we use as a measure for the spatial resolution of the sensor. The spatial resolution is mostly limited by the distance between the sample and the sensor. The diamond thickness sets the minimum distance to the sample. To decrease the distance between the sensor and the imaged sample, a thinner diamond sample or a diamond with a shallow implanted N-V layer could be used. Close proximity would increase measurement contrast and therefore the spatial resolution and allow the imaging of smaller objects.

Using the high bandwidth and spatial resolution of the device, we are able to image intricate structures on printed circuit boards (PCBs). Figure 6 shows a miniature coat of

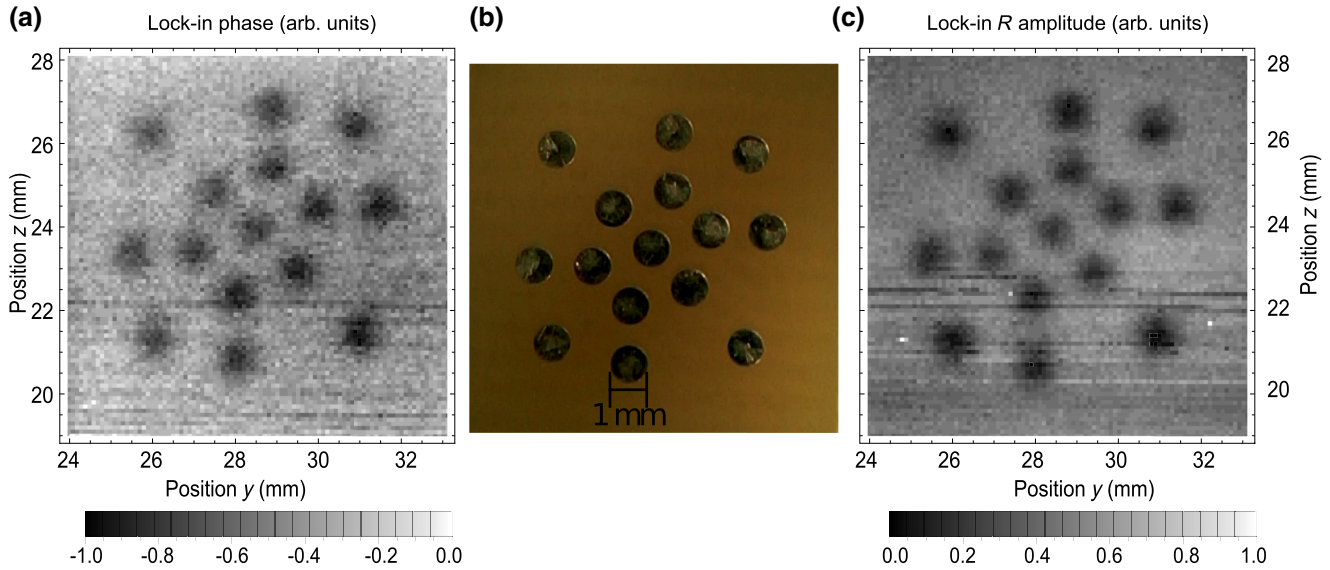

FIG. 4. (a),(c) Lock-in phase and lock-in R amplitude for a PCB containing 15 aluminum dots imaged with the eddy current. (b) Photograph of the PCB with the corresponding length of 1 mm noted for scale.

arms of the city of Mainz as imaged by the eddy-current-based method. The coat of arms is printed on a PCB made of copper with 35-μm thickness.

V. SENSITIVITY

To calculate the sensitivity of the device, we have to make assumptions about the sample to be imaged. We assume a primary field $B_{\text{prim}} = 91\ \mu\text{T}$ with frequency of 3.5 MHz and a cylindrical material with radius $r_0 = 1$ mm and height $h = 0.1$ mm (volume approximately 0.3 mm^3). The sensor is placed at a distance $d = 0.5$ mm from the material. We calculate the minimum conductivity σ that the material should have for it to produce a field strong enough to be detected with our magnetic field sensor (current sensitivity approximately 10 $\mu\text{T}/\sqrt{\text{Hz}}$).

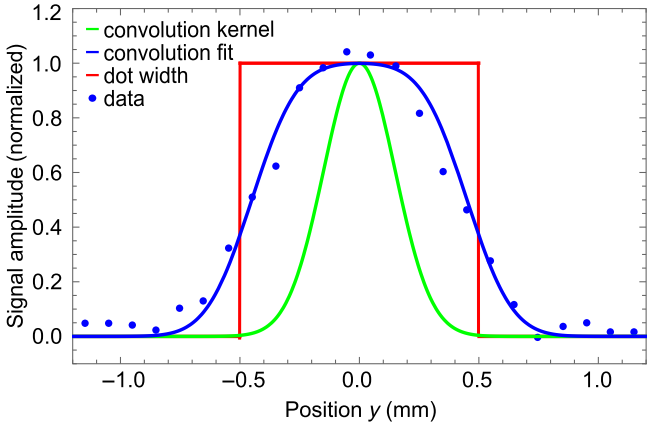

FIG. 5. Determination of spatial resolution. The blue dots signify the average cross section of 15 1-mm disks imaged by the sensor, the red plot signifies the disks' width as a square function, the green trace represents a Gaussian function needed as a kernel to recreate the experimental data, and the blue trace represents the convolution result for the red and green traces.

The secondary magnetic field can be calculated with the expression for the electromotive force:

$$U = -\frac{\Delta\Phi}{\Delta t} = -2E\pi r, \tag{1}$$

where $\Delta\Phi$ is the magnetic flux, $1/\Delta t = \omega = 2\pi f$, f being the modulation frequency of B_{prim}, E is the electric field, and r is the distance from the center of the imaged sample. With use of the Biot-Savart law, the field produced by the eddy currents (i.e., secondary field, B_{sec}) and the minimum σ able to be detected can be calculated. For the example presented, the latter would be approximately 8×10^5 S/m$\sqrt{\text{Hz}}$, and small pieces of materials such as copper and aluminum ($\sigma_{\text{Cu}} = 5.96 \times 10^7$ S/m, $\sigma_{\text{Al}} = 3.77 \times 10^7$ S/m) will be visible with our sensor.

VI. DISCUSSION

We demonstrate eddy-current imaging using N-V centers in diamond. The magnetic sensitivity is achieved with an all-optical method that is robust to misalignment and makes use of the N-V-N-V cross-relaxation feature in the PL as a function of the magnetic field. The bandwidth extends to 3.5 MHz. The spatial resolution is 348 $\mu\text{m} \pm 2\ \mu$m. The sensitivity of the device is calculated as 8×10^5 S/m$\sqrt{\text{Hz}}$ at 3.5 MHz for a cylindrical sample with radius $r_0 = 1$ mm and height $h = 0.1$ mm (volume approximately 0.3 mm^3) at a distance of 0.5 mm. With the above characteristics, our device can be used to distinguish

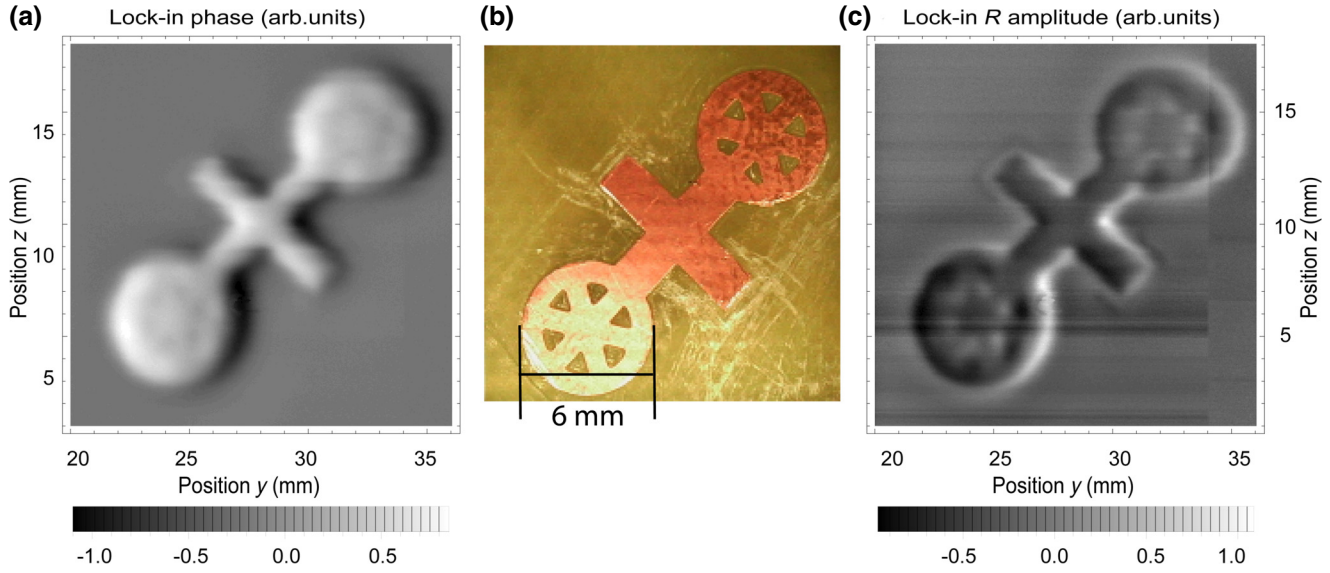

FIG. 6. (a),(c) Lock-in θ and R of a PCB depicting the coat of arms of the city of Mainz imaged with the eddy current. (b) Photograph of the PCB with the corresponding length of 6 mm noted for scale.

between different materials, detect structural defects, and image complex structures on PCBs. The technique can be further improved by closer proximity to the imaged sample, which can be achieved with a thinner diamond or one with a shallow implanted N-V layer. Compared with measurements with atomic vapor cells, the current N-V-based method has greater bandwidth and spatial resolution. Compared with coil-based commercial devices, has greater bandwidth [e.g., Zetec MIZ-22, bandwidth 50 Hz to 2 MHz and sensitivity (5×10^5 S/m)].

With the devices high bandwidth and spatial resolution, if combined with state-of-the-art N-V sensors [11,12], the sensitivity (on the order of 10 pT/$\sqrt{\text{Hz}}$) would be sufficient for applications in biomedicine to distinguish between different tissues, or even healthy and unhealthy tissues, because of their different conductivities (ranging from 0.5 to 13.7 mS/cm) [21]. The device's robustness to misalignment and its small size would allow it to be implemented in a handheld, small, and portable endoscopic sensor.

ACKNOWLEDGMENTS

The authors acknowledge support by the EU FET-OPEN Flagship Project ASTERIQS (Action No. 820394), the German Federal Ministry of Education and Research (BMBF) within the Quantumtechnologien program (Grant No. FKZ 13N14439), and the DFG through the DIP program (Grant No. FO 703/2-1). G.C. acknowledges support by internal funding from Johannes Gutenberg-Universität Mainz. L.B. is supported by a Marie Curie Individual Fellowship within the second Horizon 2020 Work Programme. H.Z. is a recipient of a fellowship through GRK Symmetry Breaking (Grant No. DFG/GRK 1581). We thank N.L. Figueroa for fruitful discussions.

[1] L. Marmugi and F. Renzoni, Optical magnetic induction tomography of the heart, Sci. Rep. **6**, 23962 (2016).

[2] C. Deans, L. Marmugi, and F. Renzoni, Active underwater detection with an array of atomic magnetometers, Appl. Optics **57**, 2346 (2018).

[3] S. Hussain, L. Marmugi, C. Deans, and F. Renzoni, Electromagnetic imaging with atomic magnetometers: A novel approach to security and surveillance, SPIE 9823, Detection and Sensing of Mines, Explosive Objects, and Obscured Targets XXI, 98230Q, 9823 (2016).

[4] G. D'Angelo and S. Rampone, Shape-based defect classification for non destructive testing IEEE Metrology for Aerospace (MetroAeroSpace) **08**, 406 (2015).

[5] A. Wickenbrock, S. Jurgilas, A. Dow, L. Marmugi, and R. Renzoni, Magnetic induction tomography using an all-optical ^{87}Rb atomic magnetometer, Optics Lett. **39**, 6367 (2014).

[6] L. Marmugi, S. Hussain, and F. Renzoni, Electromagnetic Induction Imaging with a Radio-Frequency Atomic Magnetometer, Appl. Phys. Lett. **108**, 103503 (2016).

[7] A. Wickenbrock, N. Leefer, J. W. Blanchard, and D. Budker, Eddy Current Imaging with an Atomic Radio-Frequency Magnetometer, Appl. Phys. Lett. **108**, 183507 (2016).

[8] G. Balasubramanian, I. Y. Chan, R. Kolesov, M. Al-Hmoud, J. Tisler, C. Shin, C. Kim, A. Wojcik, P. R. Hemmer, A. Krueger, T. Hanke, A. Leitenstorfer, R. Bratschitsch, F. Jelezko, and J. Wrachtrup, Nanoscale imaging magnetometry with diamond spins under ambient conditions, Nature **455**, 648 (2008).

[9] J. R. Maze, P. L. Stanwix, J. S. Hodges, S. Hong, J. M. Taylor, P. Cappellaro, L. Jiang, M. V. G. Dutt, E. Togan, A. S. Zibrov, A. Yacoby, R. L. Walsworth, and M. D. Lukin, Nanoscale magnetic sensing with an individual electronic spin in diamond, Nature **455**, 644 (2008).

[10] E. Rittweger, K. Y. Han, S. E. Irvine, C. Eggeling, and S. W. Hell, Sted microscopy reveals crystal colour centres with nanometric resolution, Nat. Photonics **3**, 144 (2009).

[11] J. F. Barry, M. J. Turner, J. M. Schloss, D. R. Glenn, Y. Song, M. D. Lukin, H. Park, and R. L. Walsworth, Optical magnetic detection of single-neuron action potentials using quantum defects in diamond, PNAS **113**, 14133 (2016).

[12] G. Chatzidrosos, A. Wickenbrock, L. Bougas, N. Leefer, T. Wu, K. Jensen, Y. Dumeige, and D. Budker, Miniature Cavity-enhanced Diamond Magnetometer, Phys. Rev. Appl. **8**, 044019 (2017).

[13] Y. Dumeige, M. Chipaux, V. Jacques, F. Treussart, J.-F. Roch, T. Debuisschert, V. M. Acosta, A. Jarmola, K. Jensen, P. Kehayias, and D. Budker, Magnetometry with nitrogen-vacancy ensembles in diamond based on infrared absorption in a doubly resonant optical cavity, Phys. Rev. B **87**, 155202 (2013).

[14] H. Zheng, G. Chatzidrosos, A. Wickenbrock, L. Bougas, R. Lazda, A. Berzins, F. H. Gahbauer, M. Auzinsh, R. Ferber, and D. Budker, Level anti-crossing magnetometry with color centers in diamond, Proc. SPIE, **10119**, 101190X-1 (2017).

[15] A. Wickenbrock, H. Zheng, L. Bougas, N. Leefer, S. Afach, A. Jarmola, V. M. Acosta, and D. Budker, Microwave-Free Magnetometry with Nitrogen-Vacancy Centers in Diamond, Appl. Phys. Lett. **109**, 5 (2016).

[16] S. Armstrong, L. J. Rogers, R. L. McMurtrie, and N. B. Manson, NV-NV electron-electron spin and NV-NS electron-electron and electron-nuclear spin interaction in diamond, Phys. Procedia **3**, 1569 (2010). Proceedings of the Tenth International Meeting on Hole Burning, Single Molecule and Related Spectroscopies: Science and Applications-HBSM 2009.

[17] L. T. Hall, P. Kehayias, D. A. Simpson, A. Jarmola, A. Stacey, D. Budker, and L. C. L. Hollenberg, Detection of nanoscale electron spin resonance spectra demonstrated using nitrogen-vacancy centre probes in diamond, Nat. Commun. **7**, 10211 (2016).

[18] S. V. Anishchik and K. L. Ivanov, Level-crossing spectroscopy of nitrogen-vacancy centers in diamond: Sensitive detection of paramagnetic defect centers, Phys. Rev. B **96**, 115142 (2017).

[19] J. D. A. Wood, D. A. Broadway, L. T. Hall, A. Stacey, D. A. Simpson, J.-P. Tetienne, and L. C. L. Hollenberg, Wide-band nanoscale magnetic resonance spectroscopy using quantum relaxation of a single spin in diamond, Phys. Rev. B **94**, 155402 (2016).

[20] L. Marmugi, C. Deans, and R. Renzoni, Atomic magnetometry-based electromagnetic imaging of low-conductivity semiconductors, arXiv:1805.05743 (2018).

[21] K. Foster and J. Schepps, Dielectric properties of tumor and normal tissues at radio through microwave frequencies, J. Microwave Power **16**, 107 (1981).